

Supporting Information

CMOS-Integrable Ambipolar Tellurene nanofilm-based Negative Differential Transconductance Transistor for Multi-Valued Logic Computing

Jihoon Huh^{ab}, Bolim You^{ab}, Yuna Kim^a, Mino Yang^c, Unjeong Kim^{d*}, Myung Gwan Hahm^{ae*},
Min-Kyu Joo^{fg*}, Moonsang Lee^{ab*}

^a Department of Materials Science and Engineering, Inha University, 100 Inha-ro, Michuhol-gu, Incheon 22212, Republic of Korea

^b Program in Semiconductor Convergence, Inha University, 100 Inha-ro, Michuhol-gu, Incheon 22212, Republic of Korea

^c Korea Basic Science Institute Seoul, 6-7, Goryeodae-ro 22-gil, Seongbuk-gu, Seoul 02841, Republic of Korea

^d Department of physics, Dongguk university, Seoul 04620, republic of korea

^e Institute for Bio-Medical and Translational Health Care, Inha University Hospital, 27 Inhang-ro, Jung-gu, Incheon 22332, Republic of Korea

^f Department of Applied Physics, Sookmyung Women's University, Seoul 04310, Republic of Korea

^g Institute of Advanced Materials and Systems, Sookmyung Women's University, Seoul 04310, Republic of Korea

* Corresponding authors.

E-mail addresses: ujjane.kim@dongguk.edu (U. Kim), mghahm@inha.ac.kr (M.G. Hahm),
mkjoo@sookmyung.ac.kr (M.-K. Joo), mslee@inha.ac.kr (M. Lee)

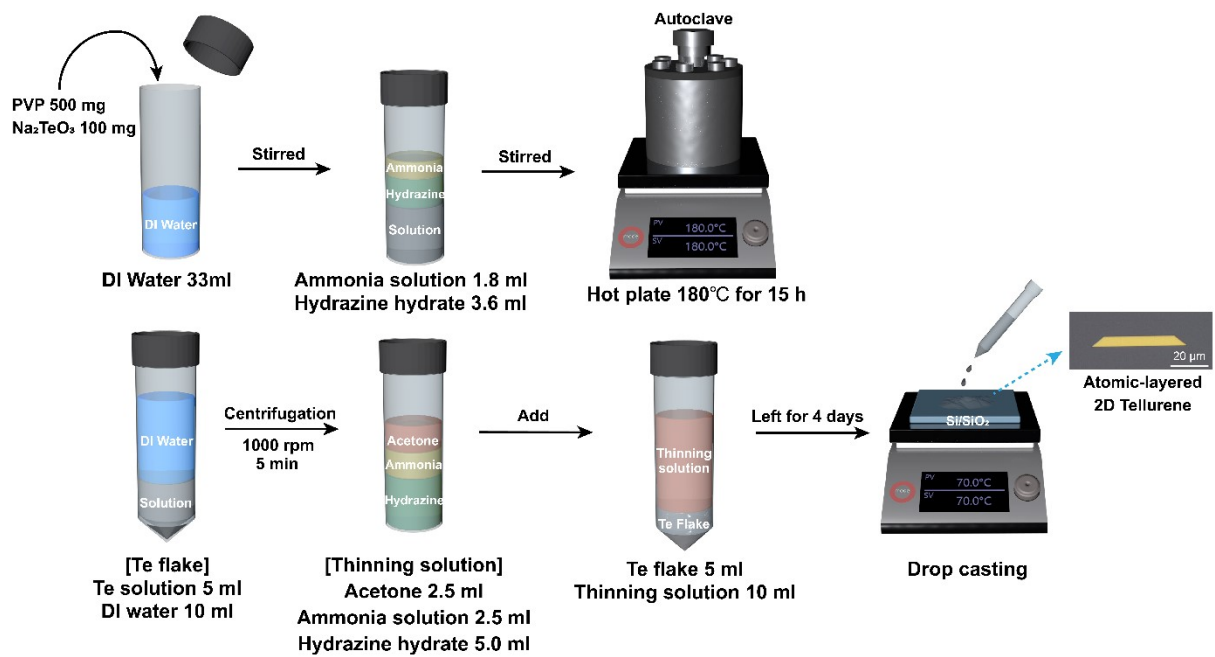
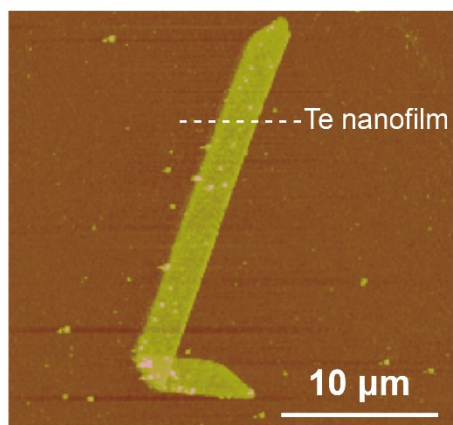


Figure S1. Schematic of the hydrothermal process for synthesizing atomic-layered tellurene (Te) using solvent-assisted thinning, followed by drop casting.

a



b

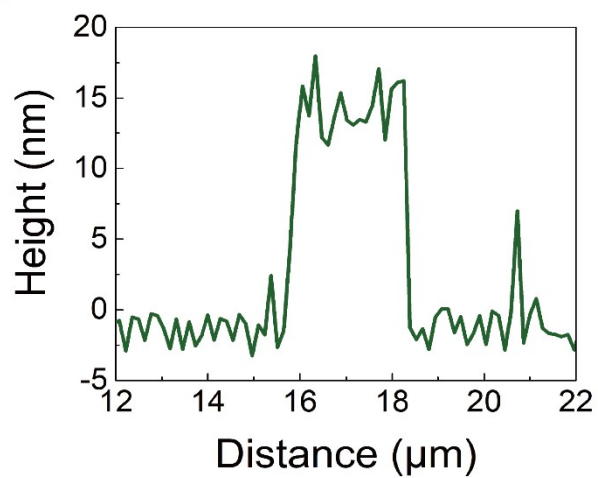


Figure S2. (a) The atomic force microscopy (AFM) image of the Te nanofilm and b) its corresponding height profile along the dashed white line, indicating a thickness of approximately 16.2 nm.

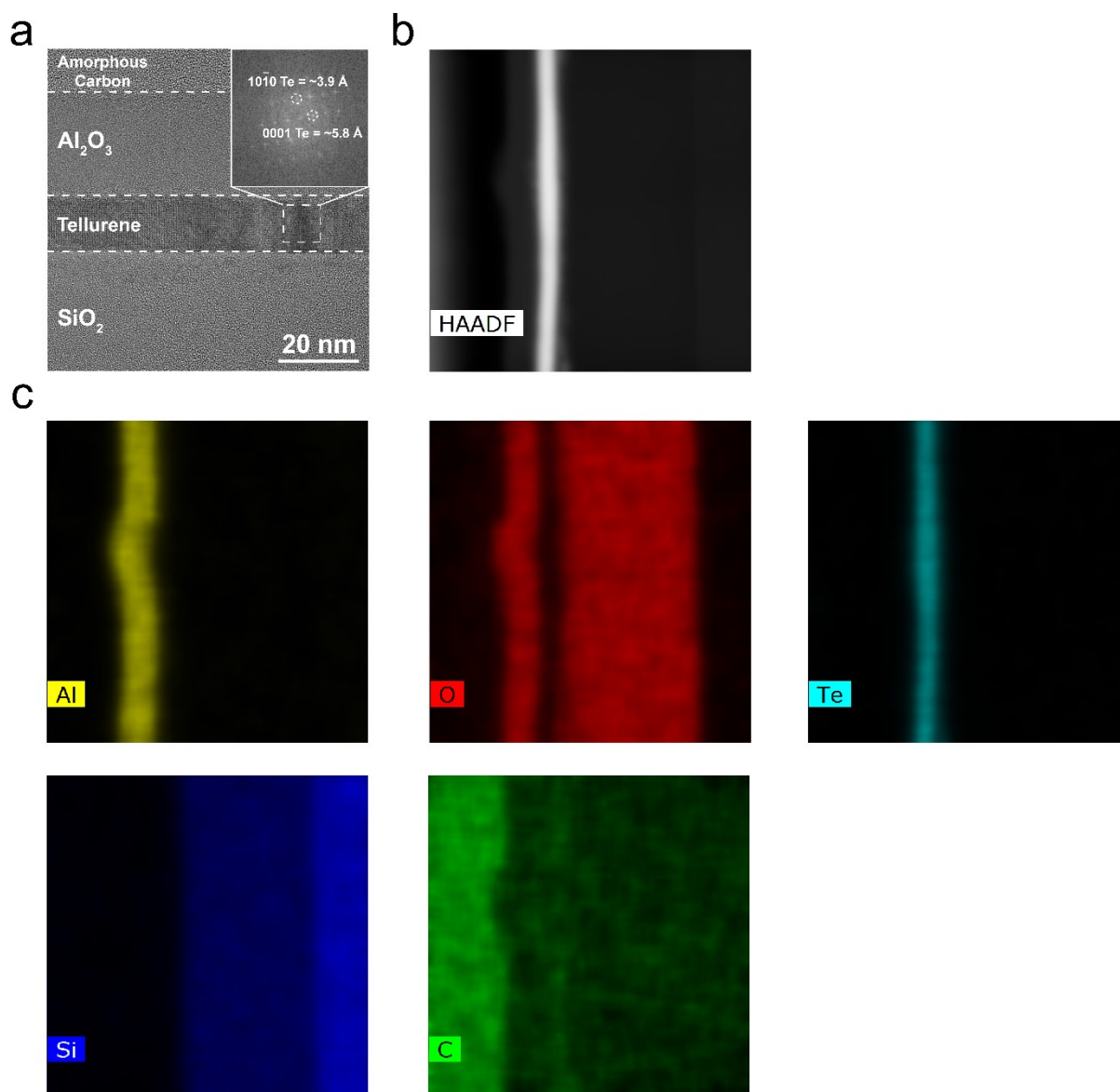


Figure S3. (a) Cross-sectional HRTEM image of Te nanoflake on a Si/SiO₂ substrate, covered with a thin Al₂O₃ film; inset: FFT pattern obtained from the Te nanoflake. (b) High-angle annular dark-field scanning transmission electron microscopy (HAADF-STEM) image of Te on a Si/SiO₂ substrate with a 20 nm Al₂O₃ layer. (c) EDS mapping images showing the distribution of Al, O, Te, Si, and amorphous carbon.

The successful fabrication of an ambipolar transistor with the Al₂O₃/Te/SiO₂/Si structure was demonstrated through cross-sectional high-resolution transmission electron microscopy (HRTEM) imaging (**Figure S3a**). The fast Fourier transform (FFT) pattern (depicted in the inset of **Figure S3a**) revealed the diffraction pattern of Te alongside the SiO₂/Si substrate, with the interplanar distance of the Te (10 $\bar{1}$ 0) and (0001) planes measured to be approximately 3.9

and 5.8 Å, respectively. This observation aligns with those of previous studies, demonstrating the successful synthesis of atomically thin Te nanofilm.¹ High-angle annular dark-field scanning transmission electron microscopy (HAADF-STEM) and energy-dispersive spectroscopy (EDS) mapping were employed to further analyze the atomic compositions of the fabricated structure (**Figure S3b, c**). The results clearly indicate that the Al₂O₃ thin film was successfully deposited onto the Te nanoflake *via* the atomic layer deposition (ALD) process.

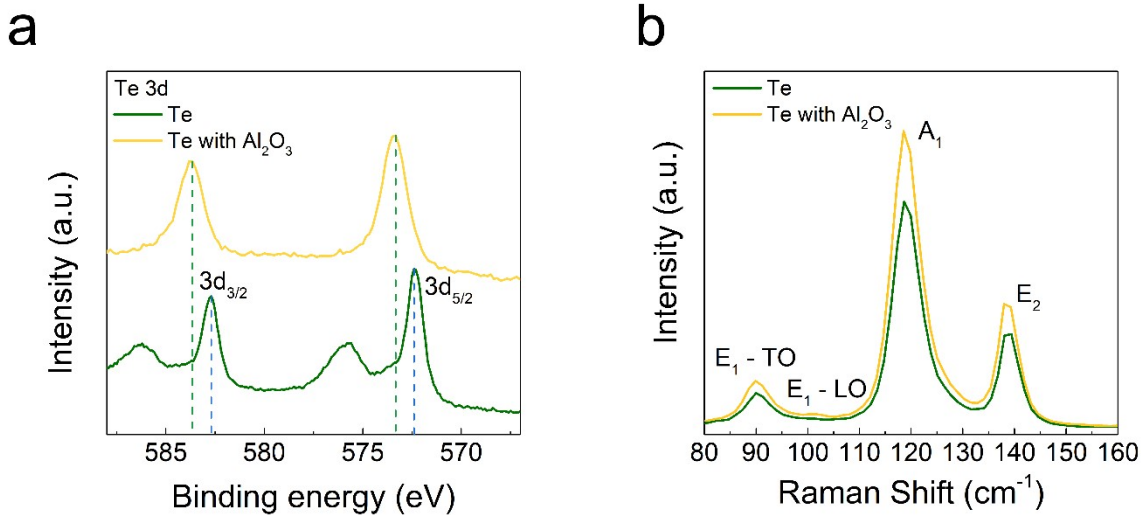


Figure S4. (a) Te 3d X-ray photoelectron (XPS) spectra of the bare Te and Te with Al₂O₃ thin film. (b) Raman spectra of bare Te and Al₂O₃ on Te.

To analyze the changes caused by the deposition of the Al₂O₃ encapsulation layer, we compared the Te before and after the Al₂O₃ encapsulation using X-ray photoelectron spectroscopy (XPS) and Raman spectroscopy. **Figure S4a** depicts the 3d XPS spectra of the synthesized Te before (green) and after (yellow) Al₂O₃ deposition, calibrated to the adventitious carbon (C_{1s}) core level peak. The Te 3d_{5/2} and Te 3d_{3/2} peaks of bare Te are located at 572.4 and 582.7 eV, respectively, which shift to higher binding energies of 573.3 and 583.7 eV, respectively, after the Al₂O₃ deposition. Since the XPS spectrum is determined by the energy position of the Fermi level of the material, this shift towards higher binding energies indicates that the chemical potential of Te moves towards the conduction band due to the Al₂O₃ deposition, demonstrating the n-doping effect of Al₂O₃ encapsulation.^{2,3} Additionally, the disappearance in the intensity of the Te⁴⁺ 3d_{5/2} and Te⁴⁺ 3d_{3/2} peaks is attributed to the reduction of oxygen in the subsurface Te layer, facilitated by the reducing action of trimethylaluminum (TMA) during the growth of Al₂O₃ *via* the ALD process.⁴ **Figure S4b** depicts the Raman spectra of the synthesized Te before (green) and after (yellow) Al₂O₃ encapsulation, measured under a 532 nm laser excitation. Four major Raman-active modes are observed at 90.4, 101.7, 119.0, and 139.0 cm⁻¹, corresponding to the E₁ transverse optical (TO) mode, the E₁ longitudinal optical (LO) phonon mode, the A₁ mode, and the E₂ mode, respectively. These peaks exhibit good concurrence with those reported in previous studies.¹ Notably, a broad E₁ LO peak is observed in the Te with a

thickness below 10 nm, which is attributed to the deformation potential in the Te lattice. Following Al₂O₃ deposition, a redshift of approximately 0.2 cm⁻¹ is observed in the Raman spectra, with the peaks shifting to 90.2, 101.6, 118.9, and 138.8 cm⁻¹, respectively. This redshift indicates that the electron concentration induced by the n-doping effect from oxygen vacancies at the Te interface, caused by the Al₂O₃ deposition, weakens the Raman vibrations. Similar shifts in the Raman peaks after Al₂O₃ deposition have been reported in transition metal dichalcogenides (TMDCs) in previous studies.⁵⁻⁸

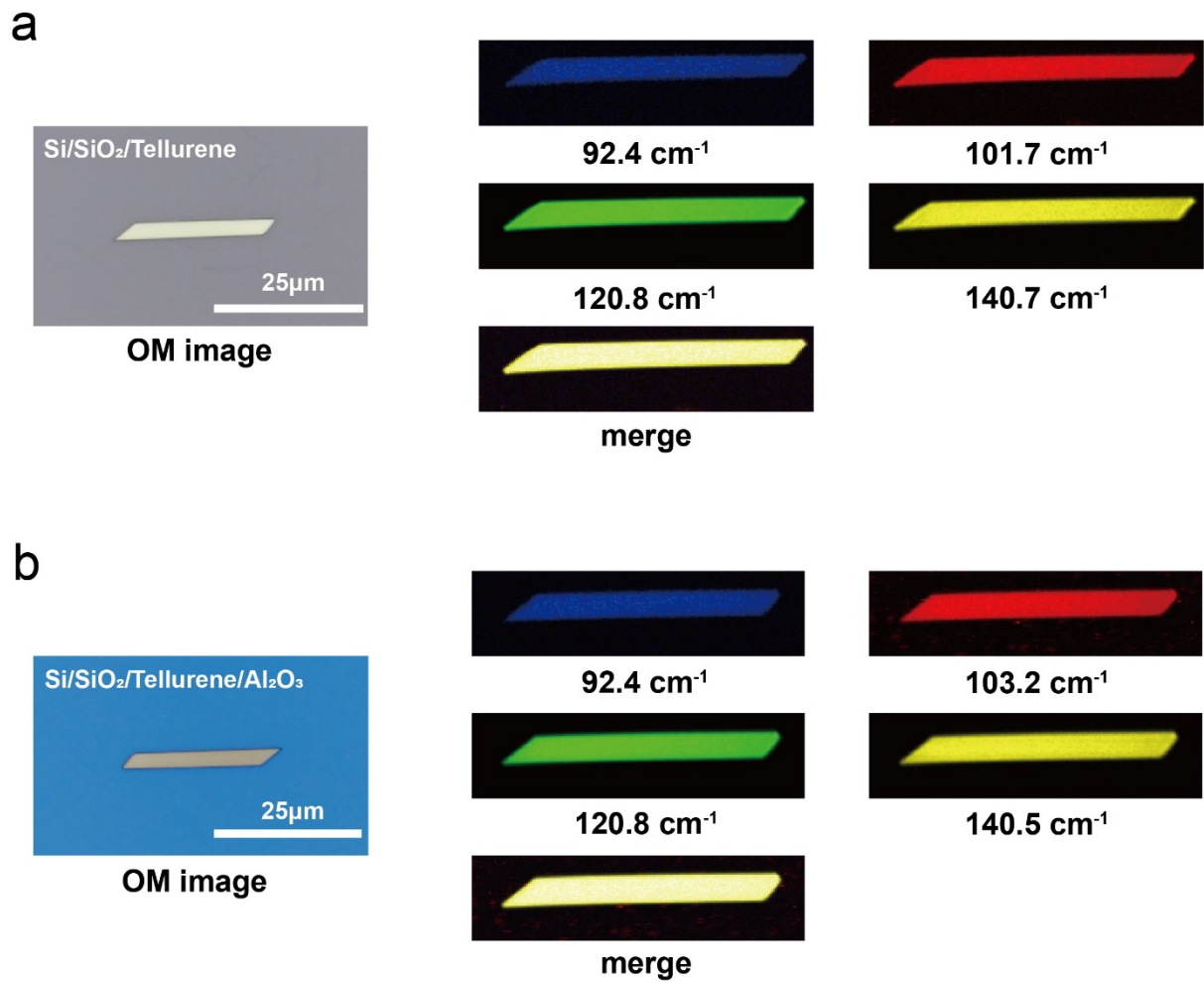


Figure S5. (a) Optical and Raman mapping images of a bare Te transferred on the Si/SiO₂ (100 nm) substrate. (b) Optical and Raman mapping images of Te with a 20 nm-thick Al₂O₃ layer deposited on the Si/SiO₂ (100 nm) substrate.

The uniform distribution of the Raman spectral intensity before and after Al₂O₃ encapsulation, observed *via* Raman mapping, demonstrates that the synthesized Te flakes exhibit consistent crystal quality across their entire surface and that Al₂O₃ was uniformly deposited on the Te surface.

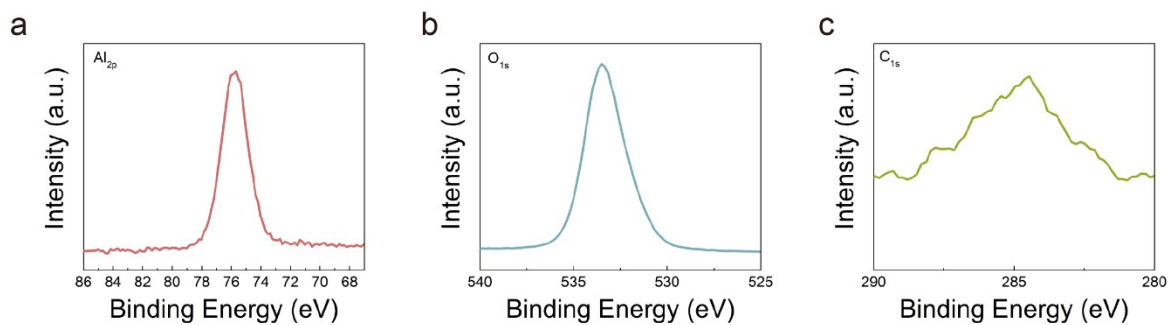


Figure S6. XPS core level spectra of (a) Al_{2p}, (b) O_{1s}, and (c) C_{1s} for Al₂O₃ on Te.

Table S1. Atomic percentages for Al, O, and C of Al₂O₃ on Te. The obtained O/Al ratio of 1:1.46 indicates an oxygen deficiency in Al₂O₃ using ALD.

	Peak Binding energy (eV)	Intensity (CPS)	FWHM (eV)	Area under curve	Atomic percentage (%)
Al _{2p}	75.7	1065.5	2.15	2056.9	40.25
O _{1s}	533.5	16252.1	2.50	43917.5	58.75
C _{1s}	284.8	531.38	3.39	467.2	0.86

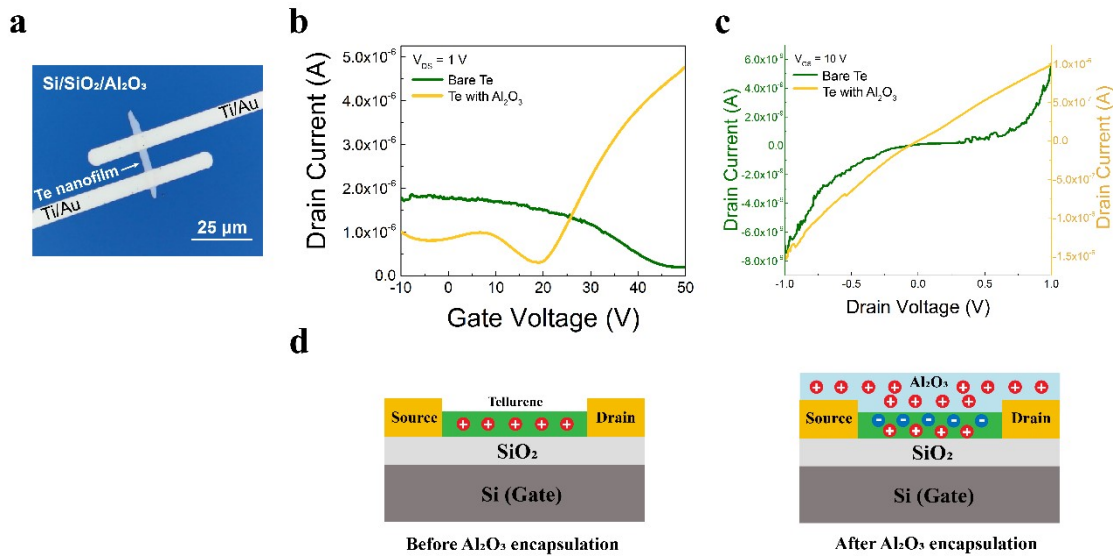


Figure S7. (a) Optical image of the fabricated ambipolar Te FET with Al₂O₃ thin film deposition. (b) Transfer and (c) output curves of bare Te when compared with Te with a 20 nm-thick Al₂O₃ layer. (d) Schematic of Te FETs with bare Te and 20 nm Al₂O₃-encapsulated Te.

As shown in **Figure S7a**, we fabricated a back-gate Te FET with a channel length of 8.9 μm and a width of 3.2 μm using Ti/Au (30/50 nm) as source/drain electrodes. To modulate the p-type Te to exhibit ambipolar characteristics, an Al₂O₃ thin film with a thickness of 20 nm was deposited *via* ALD, encapsulating the Te surface. A comparative analysis of the transfer and output characteristics was conducted before and after the deposition of the Al₂O₃ thin film. In **Figure S7b**, the transfer curves for the pristine (green) and Al₂O₃-encapsulated (yellow) Te devices are depicted at $V_{DS} = 1$ V. Before encapsulation, the device exhibits typical p-type characteristics (green), with the increase in I_{DS} as V_{GS} is swept from 50 V to -10 V. Conversely, after the deposition of the 20 nm Al₂O₃ thin film (yellow), the device exhibits clear ambipolar characteristics, indicating successful modulation due to the encapsulation process. **Figure S7c** highlights the output characteristics at $V_{GS} = 10$ V. After the Al₂O₃ layer was applied, the output curve (yellow) demonstrates a linear behavior, indicating a reduced Schottky barrier between the Te and Ti/Au electrodes. Following encapsulation, the current level increased by nearly 180 times, indicating that the Fermi level shift in the Te reduced the effective Schottky barrier for electron injection, leading to activated n-type behavior. Thus, ambipolar behavior, with symmetric injection barriers for both electrons and holes, was successfully realized. The formation of oxygen vacancies within the interface of the Al₂O₃ layer leads to positive fixed

charges, generating donor states near the conduction band of Te, as shown in **Figure S7d**.^{9, 10} These changes in electron concentration shift the Fermi level and affect the band alignments. When the concentrations of electrons and holes become comparable, the Fermi level settles between the conduction and valence bands, causing the device to demonstrate ambipolar behavior. This modulation of ambipolarity *via* Al₂O₃ deposition has been reported in other studies as well, confirming the consistency of this approach in improving the ambipolar characteristics.^{10, 11}

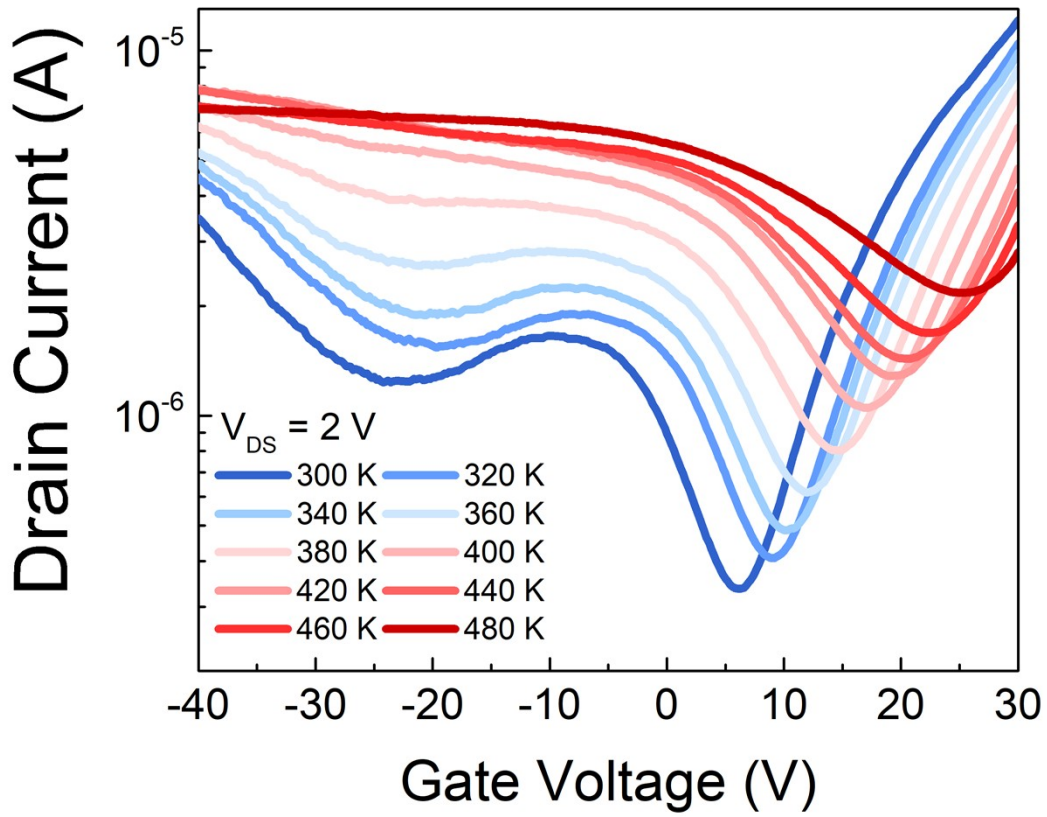


Figure S8. Temperature-dependent transfer characteristics of the Te ambipolar FET from 300 to 480 K with diminishing NDT effects at higher temperatures.

References

1. Y. Wang, G. Qiu, R. Wang, S. Huang, Q. Wang, Y. Liu, Y. Du, W. A. Goddard III, M. J. Kim and X. Xu, *Nature Electronics*, 2018, **1**, 228-236.
2. M. Li, D. Gao, S. Li, Z. Zhou, J. Zou, H. Tao, L. Wang, M. Xu and J. Peng, *RSC advances*, 2015, **5**, 104613-104620.
3. C. Guerra-Nuñez, M. Döbeli, J. Michler and I. Utke, *Chemistry of Materials*, 2017, **29**, 8690-8703.
4. T. Kim, C. H. Choi, P. Byeon, M. Lee, A. Song, K.-B. Chung, S. Han, S.-Y. Chung, K.-S. Park and J. K. Jeong, *npj 2D Materials and Applications*, 2022, **6**, 4.
5. K. Chen, D. Kiriya, M. Hettick, M. Tosun, T.-J. Ha, S. R. Madhvapathy, S. Desai, A. Sachid and A. Javey, *Apl Materials*, 2014, **2**.
6. C. J. L. de la Rosa, A. Nourbakhsh, M. Heyne, I. Asselberghs, C. Huyghebaert, I. Radu, M. Heyns and S. De Gendt, *Nanoscale*, 2017, **9**, 258-265.
7. Y. J. Park, A. K. Katiyar, A. T. Hoang and J. H. Ahn, *Small*, 2019, **15**, 1901772.
8. T. Das, S. Youn, J. E. Seo, E. Yang and J. Chang, *ACS Applied Materials & Interfaces*, 2023, **15**, 45116-45127.
9. Y. M. Chang, S. H. Yang, C. Y. Lin, C. H. Chen, C. H. Lien, W. B. Jian, K. Ueno, Y. W. Suen, K. Tsukagoshi and Y. F. Lin, *Advanced Materials*, 2018, **30**, 1706995.
10. D. A. Nguyen, S. Cho, S. Park, D. Y. Park, H. C. Suh, M. S. Jeong, T. P. A. Bach, H. Kim and H. Im, *Nano Energy*, 2023, **113**, 108552.
11. M. Cheong, D. Choi, B. You, Y. Kim, Y. Han, T. Kim, C. Ko, J. L. MacManus-Driscoll, A. J. Flewitt and U. J. Kim, *ACS Applied Electronic Materials*, 2024, **6**, 8532-8539.